The Cryosphere Discuss., 8, 1631–1671, 2014
www.the-cryosphere-discuss.net/8/1631/2014/
doi:10.5194/tcd-8-1631-2014

The Cryosphere
Discussions
Open Access

Combining damage and fracture mechanics to model calving

J. Krug[1,2], J. Weiss[1,2], O. Gagliardini[1,2,3], and G. Durand[1,2]

[1]CNRS, LGGE, 38041 Grenoble, France
[2]Univ. Grenoble Alpes, LGGE, 38041 Grenoble, France
[3]Institut Universitaire de France, Paris, France

Received: 4 March 2014 – Accepted: 13 March 2014 – Published: 24 March 2014

Correspondence to: J. Krug (jean.krug@ujf-grenoble.fr)

Published by Copernicus Publications on behalf of the European Geosciences Union.

Abstract

Calving of icebergs is a major negative component of polar ice-sheet mass balance. We present a new calving modeling framework relying on both continuum damage mechanics and linear elastic fracture mechanics. This combination accounts for both the slow sub-critical surface crevassing and fast propagation of crevasses when calving occurs. First, damage of the ice occurs over long timescales and enhances the viscous flow of ice. Then brittle fracture propagation happens downward, over very short timescales, in ice considered as an elastic medium. The model is validated on Helheim Glacier, South-West Greenland, one of the most monitored fast-flowing outlet glacier. This allows to identify sets of model parameters giving a consistent response of the model and producing a dynamic equilibrium in agreement with observed stable position of the Helheim ice front between 1930 and today.

1 Introduction

Over the last decades, discharge of ice from Greenland and Antarctic ice sheets strongly increased (Shepherd et al., 2012), due to either a larger submarine melting, or an increasing rate of calving. Recent observations have shown that the ice loss is, in average, equally distributed between these two sink terms despite some regional differences (Rignot et al., 2010; Depoorter et al., 2013). Ice loss by iceberg calving has been evaluated to 1321 ± 144 gigatonnes per year for Antarctica in 2013 (Depoorter et al., 2013) and 357 gigatonnes per year for Greenland between 2000 and 2005 (Rignot and Kanagaratnam, 2006). These figures could become more important, as the front destabilization can exert a strong positive feedback on glacier dynamics. Indeed, the abrupt collapse of the front can destabilize the whole glacier, leading to both the thinning and so the acceleration of upstream ice through the loss of buttressing, and thus increasing again the discharge (Gagliardini et al., 2010). The collapse of Larsen B ice shelf in 2002 (Scambos et al., 2004) or the disintegration of the floating tongue of

Jakobshavn Isbrae, on the West coast of Greenland ice sheet the same year (Joughin et al., 2008a) are two examples of the impact of such perturbations on the behaviour of a glacier. In the sake of projecting ice sheet evolution, a deep understanding and representation of the processes occurring at the front are necessary, especially those concerning iceberg calving.

Among the several studies undertaken to model calving, the most used criterion is the one proposed by Nye (1957), according to whom the ability for a glacier to calve depends on the equilibrium between longitudinal stretching (opening term) and cryostatic pressure (closing term). This criterion has been used by several authors (e.g. Mottram and Benn, 2009; Nick et al., 2010; Otero et al., 2010; Nick et al., 2013) with successful results in representing the front variations of some major greenlandic and antarctic outlet glaciers. However, this model is based on a simple stress balance combined to an empirical criterion for calving. Consequently, it does not account for some physical aspects, such as the stress concentration at the tip of crevasses, or the crevasse depth, and so it may assess inaccurately the ice discharge in case of prognostic simulations.

Another approach to model calving has been done using particles models (Bassis and Jacobs, 2013; Åström et al., 2013). These models show interesting behaviours on describing the calving processes and the iceberg distribution, but are today inappropriate to describe large-scale ice-sheet flow due to their non-continuous approach.

For a few years, some authors have focused on continuum damage mechanics in order to represent both the development of micro-defects in the ice to the apparition of macro-scale crevasses, and their effects on the viscous behaviour of the ice while keeping a continuum approach. Initially applied to the deformation of metals (Kachanov, 1958), damage mechanics has been recently applied to ice dynamics to study the apparition of a single crevasse (Pralong et al., 2003; Pralong and Funk, 2005; Duddu and Waisman, 2013) or to average crevasse fields (Borstad et al., 2012). On the other hand, the elastic representation of fracturing processes using linear elastic fracture mechanics (van der Veen, 1998a, b) has been employed to described the calving event itself, characterized by a rapid propagation of surface and bottom crevasses through the ice.

TCD
8, 1631–1671, 2014

This approach has been rarely used in ice-sheet numerical modeling, however, as the representation of crevasses requires a high mesh refinement usually difficult to reach when modeling large glaciological bodies.

Here we consider a combined approach between damage mechanics and fracture mechanics. The proposed physically-based calving model can cover both the accumulation of damage as the ice is transported through the glacier, and the critical fracture propagation in the vicinity of the calving front. The slow development of damage represents the long timescales evolution of purely viscous ice, while the use of fracture mechanics allows to consider calving events occurring at short timescales, for which the ice can be considered as a purely elastic medium. The description of the physics implemented is presented in Sect. 2, covering the damage initiation and its development, the fracture propagation and its arrest criterion. In Sect. 3, sensitivity tests are carried on Helheim Glacier, and results are discussed.

2 Physics of the model

2.1 Governing equations for ice flow

2.1.1 Ice flow and rheology

We consider an incompressible, isothermal and gravity-driven ice-flow in which the ice exhibits a non-linear viscosity. The ice flow is ruled by the Stokes equations (i.e. Navier–Stokes equations without any inertial term), meaning the momentum and the mass balance:

$$\mathrm{div}(\boldsymbol{\sigma}) + \rho_{\mathrm{i}}\mathbf{g} = 0 \quad (1)$$

$$\mathrm{div}(\boldsymbol{u}) = 0 \quad (2)$$

where $\boldsymbol{\sigma}$ represents the Cauchy stress tensor, $\boldsymbol{g}$ the gravity force vector, ρ_{i} the density of ice and $\boldsymbol{u}$ the velocity vector. The Cauchy stress tensor can be expressed as a function of the deviatoric stress tensor **S** and the isotropic pressure p with $\boldsymbol{\sigma} = \mathbf{S} - p\mathbf{I}$ and $p = -\mathrm{tr}(\boldsymbol{\sigma})/3$. Ice rheology is represented by a non-linear Norton–Hoff type flow law called *Glen's flow* law, which reads:

$$\mathbf{S} = 2\eta\dot{\boldsymbol{\epsilon}} \tag{3}$$

This equation links the deviatoric stress tensor **S** to the strain rate tensor $\dot{\boldsymbol{\epsilon}}$. The effective viscosity η writes:

$$\eta = \frac{1}{2}(EA)^{-1/n}\mathbf{I}_{\dot{\epsilon}_2}^{(1-n)/n} \tag{4}$$

where $\mathbf{I}_{\dot{\epsilon}_2}^2$ represents the square of the second invariant of the strain rate tensor, A is the fluidity parameter and E is an *enhancement factor*, usually varying between 0.58 and 5.6 for ice-flow models (Ma et al., 2010).

2.1.2 Boundary conditions

The upper surface is defined as a stress-free surface, and therefore obeys the following equation:

$$\frac{\partial z_\mathrm{s}}{\partial t} + u_\mathrm{s}\frac{\partial z_\mathrm{s}}{\partial x} + v_\mathrm{s}\frac{\partial z_\mathrm{s}}{\partial y} - w_\mathrm{s} = a_\mathrm{s} \tag{5}$$

where z_s refers to the elevation of the top surface, and $(u_\mathrm{s}, v_\mathrm{s}, w_\mathrm{s})$ are the surface velocities. The surface mass balance a_s is prescribed as a vertical component only. As we neglect any effect of atmospheric pressure, normal and tangential stresses at the surface are zero:

$$\sigma_{nn}|_\mathrm{s} = 0$$
$$\sigma_{nt_i}|_\mathrm{s} = 0 \ (i = 1,2)$$

TCD
8, 1631–1671, 2014

Subscripts n and t_i respectively refers to normal (pointing outward) and tangential directions.

Similar to the upper free surface, the bottom surface is described by:

$$\frac{\partial z_b}{\partial t} + u_b \frac{\partial z_b}{\partial x} + v_b \frac{\partial z_b}{\partial y} - w_b = a_b \tag{6}$$

where (u_b, v_b, w_b) are the basal velocities, and a_b represents the vertical component of the basal mass balance (melting or accretion). At the bed, the glacier can be either grounded or floating. The grounded part of the glacier undergoes a shearing stress which is represented by a non-linear Weertman-type friction law reading:

$$\boldsymbol{u} \cdot \boldsymbol{n} = 0$$
$$\sigma_{nt_i}|_b = t_i \cdot (\sigma \cdot n)|_b = C u_b^{m-1} u_{t_i} \ (i = 1,2)$$

where C and $m = 1/3$ are the friction coefficient and the friction exponent respectively. u_b is the norm of the sliding velocity $\boldsymbol{u_b} = \boldsymbol{u} - (\boldsymbol{u} \cdot \boldsymbol{n_b})\boldsymbol{n_b}$, with $\boldsymbol{n_b}$ the normal outward-pointing unit vector to the bedrock. Where the ice is floating the free surface is forced by an external sea pressure normal to the surface:

$$\sigma_{nn}|_b = -\rho_w g (l_w - z_b)$$
$$\sigma_{nt_i}|_b = 0 \ (i = 1,2)$$

where ρ_w is the water density, l_w the sea level, and z_b refers to the elevation of bottom surface. The position between the grounded and floating part of the basal boundary, i.e. the grounding line, is part of the solution and computed solving a contact problem following Durand et al. (2009) and Favier et al. (2012). The basal friction C is determined using the inverse method described in Jay-Allemand et al. (2011). This method consists in inferring the basal friction parameter by reducing the mismatch between observed and modeled surface velocities.

TCD
8, 1631–1671, 2014

The front is defined as a third free-surface, which can undergo melting, and follows the equation:

$$\frac{\partial x_f}{\partial t} + v_f \frac{\partial x_f}{\partial y} + w_f \frac{\partial x_f}{\partial z} - u_f = a_f \quad (7)$$

where (u_f, v_f, w_f) are the frontal velocities, and a_f characterizes the frontal mass balance. The front undergoes water back pressure where the ice stands under sea level and a stress-free condition a.s.l. These Neumann conditions read:

$$\sigma_{nn}|_f = -\max(\rho_w g(l_w - z), 0)$$

$$\sigma_{nt_i}|_f = 0 \; (i = 1, 2)$$

The list of physical and numerical parameters used in this paper is given in Table 1. Some boundary conditions are specific to the 2-D flowline application conducted in Sect. 3. More details about these specific boundaries are given in Sect.3.2.

2.2 Continuum damage mechanics model

Continuum Damage Mechanics (CDM) was first proposed by Kachanov (1958) to quantify the degradation of mechanical properties resulting from the nucleation of internal defects such as microcracks or voids. As stated by Lemaitre et al. (1988), CDM describes the evolution of phenomena in the medium from a virgin state to the initiation of macroscopic fracture. The major interest of this approach is that the material is still considered as a continuous material, even when the level of damage is high. The slow deformation is typically encountered in glaciological media, where the ice flows slowly under its own weight along the slope of the surface. CDM has been successfully used in ice-flow models to deal with some glaciological issues such as the flow acceleration of large damaged areas or the opening of crevasses in hanging glaciers (Xiao and Jordaan, 1996; Pralong et al., 2003; Pralong and Funk, 2005; Jouvet et al., 2011; Borstad et al., 2012).

The principle of CDM models is based on the use of a damage variable, usually denoted D, which represents the degradation of mechanical properties (stiffness, viscosity,...) resulting from a population of defects whose effect is averaged at a mesoscale. When considering an anisotropic approach, damage must be represented as a second order tensor (Murakami and Ohno, 1981; Pralong and Funk, 2005). As stated by Rist et al. (1999), considering damage as isotropic is sufficient when dealing with glaciological bodies such as glaciers or ice-sheets. In this case, as it is assumed here, the state variable D is a scalar quantity. For non-damaged ice $D = 0$, and $0 < D < 1$ when ice is damaged. A fully damaged ice is obtained when $D \rightarrow 1$.

To describe the stress altered by the amount of damage, an effective stress is introduced:

$$\tilde{\boldsymbol{\sigma}} = \frac{\boldsymbol{\sigma}}{(1 - D)}, \tag{8}$$

with $\tilde{\boldsymbol{\sigma}}$ the effective Cauchy stress tensor. This effective stress can be understood as the original force applied on an effective undamaged area only. Using the equivalence principle of Lemaitre et al. (1988), strain is affected by the damage only through the effect of an effective stress entering the rheological law (see Eq. 3) at the place of $\boldsymbol{\sigma}$. Thereby, there is no need to define an effective strain rate.

2.2.1 Damage evolution

Damage is a property of the material at the mesoscale. It is therefore advected by the ice flow, and evolves through time depending on the stress field. To take this evolution into account, we prescribe an advection equation reading:

$$\frac{\partial D}{\partial t} + \boldsymbol{u}\nabla D = \begin{cases} f(\chi) & \text{if } f(\chi) > 0 \\ 0 & \text{otherwise} \end{cases} \tag{9}$$

where the right hand side represents a damage source term $f(\chi)$. This term can be written as a function of a damage criterion χ and a numerical parameter B, thereafter named *damage enhancement factor*:

$$f(\chi) = B \cdot \chi \tag{10}$$

In Sect. 3, some sensitivity experiments of the CDM model to the damage enhancement factor are presented.

The damage criterion is pivotal for the representation of damage increase, and its physical expression is a critical step in the formulation of the CDM model. Commonly used criteria are the Coulomb criterion (Vaughan, 1993), the von Mises criterion (Albrecht and Levermann, 2012), or the Hayhurst criterion (Pralong and Funk, 2005; Duddu and Waisman, 2013, 2012). However, these criteria are not necessarily relevant for the damage of ice: the Coulomb criterion is used for a representation of frictional process under compressive loading (e.g. Weiss and Schulson, 2009). The von Mises is usually a plasticity criterion (and so especially adequate to describe the plastic yield of metals and alloys), whereas the Hayhurst criterion is used for creep rupture and cavity growth (Hayhurst, 1972; Gagliardini et al., 2013a). Here, we adopt a pure-tensile criterion, described as a function of the maximum principal Cauchy stress σ_I. This choice is consistent with the fact that we want to describe crevasse opening under pure traction. This criterion would also be able to represent a broad variety of crevasses observed on glaciers, such as splashing crevasses. Anyway, the implementation of another criterion in the model would be straightforward, and would be an interesting parameter to investigate for future work. The currently-used criterion reads:

$$\chi(\sigma_\mathrm{I}, \sigma_\mathrm{th}, D) = \max\left\{0, \frac{\sigma_\mathrm{I}}{(1-D)} - \overline{\sigma_\mathrm{th}}\right\} \tag{11}$$

Here $\overline{\sigma_\mathrm{th}}$ represents an average stress threshold for damage initiation. The corresponding envelope of the damage criterion is represented in the space of Mohr circle in Fig. 1.

The mean stress threshold for damage initiation $\overline{\sigma_\mathrm{th}}$ corresponds to the overload which must be applied in order to reach the ice strength and initiate degradation. To account for sub-grid scale heterogeneity, we introduce some noise on the value of σ_{th}: $\sigma_{th} = \overline{\sigma_{th}} \pm \delta\sigma_{th}$, where $\frac{\delta\sigma_{th}}{\overline{\sigma_{th}}}$ follows a standard normal distribution with a standard deviation of 0.05. $\overline{\sigma_{th}}$ usually reaches several tens of kilo-Pascals (Pralong and Funk, 2005). Sensitivity of the model to this parameter will be discussed in Sect. 3.

This formulation of the damage criterion implies some assumptions on the behaviour of ice. In particular, the ice cannot be damaged under compression or pure shear. However, it remains consistent with the approach of Benn et al. (2007b), according to which the longitudinal stretching associated to longitudinal velocity gradients can be seen as a first order process controlling the development of crevasses in glaciers. Moreover, it is consistent with the fracture mechanics approach explained in Sect. 2.3 which considers crevasses opening in pure tension only.

2.2.2 Viscosity modification

As pointed by Pralong et al. (2003) and Pralong and Funk (2005) on alpine hanging glaciers, the ice flow is altered by the accumulation of micro-defects in the ice: damage softens the ice and accelerates the creep. This softening is taken into account through the introduction of the effective stress within Glen's law.

When introducing the effective deviatoric stress tensor $\tilde{\mathbf{S}}$ and taking into account the equivalence principle, as described in Sect. 2.2, Eq. (3) reads:

$$\tilde{\mathbf{S}} = (A)^{-1/n} \mathbf{I}_{\dot{\varepsilon}_2}^{(1-n)/n} \dot{\boldsymbol{\varepsilon}} \tag{12}$$

When combined with Eq. (8), it comes:

$$\mathbf{S} = (A)^{-1/n} (1-D) \mathbf{I}_{\dot{\varepsilon}_2}^{(1-n)/n} \dot{\boldsymbol{\varepsilon}} \tag{13}$$

TCD
8, 1631–1671, 2014

By identification with Eq. (3), one can link the enhancement factor E with the damage D, such as

$$E = \frac{1}{(1-D)^n} \tag{14}$$

It comes that for undamaged ice (meaning $D = 0$), $E = 1$, and so the flow regime is unchanged. When the damage increases ($D > 0$), $E > 1$, the viscosity of the ice is reduced, and so the velocity of the flow increases. This formulation of the enhancement factor is consistent with the expected behaviour, and it has already been used in previous studies, such as Borstad et al. (2012). The damage then evolves under the effect of the stress field, where the ice undergoes pure tension, and it exerts a positive feedback on the velocity field.

2.3 Fracture mechanics

Continuum damage mechanics is a reliable tool to deal with the degradation of ice viscosity with increasing damage over long timescales. It can be understood as a way to simulate sub-critical crevasse nucleation and propagation (Weiss, 2004) at a meso-scale, and its role on creep enhancement. However, calving events are triggered by rapid propagation of preexisting fractures, at very short timescales and speeds reaching a significant fraction of the speed of sound. Thus, this process cannot be represented by a viscous rheology (Weiss, 2004). Instead, at such short timescales, the medium should be considered as elastic. In these conditions, Linear Elastic Fracture Mechanics (LEFM) provides a useful tool to account for these features and matches pretty well with the observations done on crevasse depths (Mottram and Benn, 2009). The application of LEFM on penetration of surface crevasses, originally introduced by Smith (1976), was used by several authors since then (Rist et al., 1999; van der Veen, 1998a, b; Nath and Vaughan, 2003). Here, a LEFM model is combined to the damage model previously described to achieve the formulation of a calving law taking into account several processes occurring in the glacier. In LEFM, three modes of crack propagation can be considered: Mode I, Mode II and Mode III, which respectively refer to simple opening, sliding and tearing. In the following, only the opening mode (Mode I) is considered.

2.3.1 LEFM theory

The key physical parameter of LEFM is the stress intensity factor K. van der Veen (1998a) proposed an expression for K_I in an idealized case where the opening stress is constant in the vertical direction. For opening mode, in the coordinate system (x, y, z), K_I reads:

$$K_\mathrm{I} = \beta \sigma_{xx} \sqrt{\pi d} \tag{15}$$

where σ_{xx} is the horizontal component of the Cauchy stress tensor, d is the crevasse depth and β is a parameter depending on the geometry of the problem. The crack is considered to propagate vertically. In the ideal case introduced by van der Veen (1998a), fracture propagation was a function of the difference between the opening full stress S_{xx} resulting from horizontal velocity gradients, and the cryostatic pressure (*creep closure*) $\sigma_p = \rho_\mathrm{i} g z$ corresponding to the weight of the ice, thus, $\sigma_{xx} = S_{xx} + \rho_\mathrm{i} g z$.

However, when considering real cases, the opening term S_{xx} (and so σ_{xx}) is not constant over depth z or lateral coordinate y. Consequently, the appropriate formula to calculate the stress intensity factor for an arbitrary stress profile $\sigma_{xx}(y,z)$ applied to the crack is given by the weight functions method (Labbens et al., 1974):

$$K_\mathrm{I} = \int\limits_{y=y_l}^{y=y_r} \int\limits_{z=0}^{z=d} \beta(z,d,H)\ \sigma_{xx}(y,z)\ \mathrm{d}y\ \mathrm{d}z \tag{16}$$

where $y_l - y_r$ refers to the glacier width (see Fig. 2). This formula lays on the use of the superposition principle: in the case of linear elasticity, the value of the stress intensity factor at the tip of the crack can be seen as the sum of contributions of all individuals

TCD
8, 1631–1671, 2014

point loads along the crack length. In our case, instead of considering the value of the along-flow component of the deviatoric stress tensor at the tip of the crack, we multiplied it by the weight function $\beta(z,d,H)$ at each vertical coordinate and integrated it over the initial crevasse depth (Labbens et al., 1974). This way, the effect of a stress profile of arbitrary shape on the stress intensity factor can be taken into account.

In LEFM theory, a fracture is able to propagate downward in the ice if the stress intensity factor is higher than the fracture toughness K_{Ic}. The toughness is a property of the material and strongly depends on the porosity in the ice. Several experiments have been carried out to relate the value of K_{Ic} to this porosity (Fischer et al., 1995; Rist et al., 1996; Schulson and Duval, 2009). Among the range of values between 0.1 $\mathrm{MPa\,m^{1/2}}$ and 0.4 $\mathrm{MPa\,m^{1/2}}$, we choose a constant value of 0.2 $\mathrm{MPa\,m^{1/2}}$. Sensitivity to this value will be discussed in Sect. 3.3.4.

The weight function $\beta(z,d,H)$ depends on the geometry of the crevasse, and so it depends on the considered problem. Among the weight functions for various crack and notche geometries, that has been proposed, we use the one corresponding to an edge crack in an infinite width plate (Glinka, 1996), in two dimensions. A complete description of the weight function and an illustration of the geometry is given in Fig. 2 and Appendix A.

2.3.2 Critical damage contour and fracture initiation

From Eq. (16), it is easily understandable that an initiation of crevasse propagation requires a combination of both sufficient tensile stress and large enough initial crevasse depth to exceed fracture toughness. In our model, the size of pre-existing flaws is dictated by a contour of critical damage on the near-surface of the glacier, where damage reaches a critical value D_{c}. For application to the LEFM theory, we consider that the depth of this damaged layer corresponds to the initial crevasse depth d (see Fig. 3). One must keep in mind that this value of D_{c} is another threshold which needs to be set. The sensitivity of the model to this parameter will be tested in Sect. 3.

Compared to the work of van der Veen (1998a, b), we do not consider the presence of water-filled crevasses for the initiation of crack propagation, nor the formation of basal crevasses. It has been shown that water-filled crevasses are able to propagate the full thickness of the glacier as soon as the level of water in the crevasse exceeds several meters. Without this feature, our model is sufficient to provide a lower bound for crevasse propagation. It is worth noting, however, that the introduction of such a mechanism in our framework would be straightforward, once the water level within crevasses can be defined independently.

2.3.3 Fracture arrest

Once the conditions for fracture initiation are fulfilled, we consider that the crevasse propagates vertically. In van der Veen (1998b), crevasses propagate downward as long as the inequation $K_\mathrm{I} \geq K_\mathrm{Ic}$ is satisfied, thus assuming that $K_\mathrm{I} = K_\mathrm{Ic}$ represents both a crack propagation and a crack arrest criterion. Such arrest criterion is probably misleading, as the stress intensity factor at arrest, though non-zero, is always lower than the stress intensity factor at propagation (Ravi-Chandar and Knauss, 1984), mostly as dynamical effects have to be taken into account for the arrest condition. Therefore, following Ravi–Chandar, we use a crevasse arrest criterion: $K_\mathrm{I} < K_\mathrm{Ia}$, with $K_\mathrm{Ia} = \alpha K_\mathrm{Ic}$ and $0 < \alpha < 1$. The value of α for ice is unknown. In the following, we arbitrarily set α to 0.5. Sensitivity to this value will be discussed in Sect. 3.3.4.

In this simplified LEFM framework, calving would theoretically occur only if K_I remains larger than K_Ia down to the bottom of the glacier. However, as the result of cryostatic pressure and/or boundary conditions (hydrostatic pressure), K_I becomes negative before reaching $d = H$. To overcome this inconsistency, authors have proposed alternative criteria. Benn et al. (2007a) proposed a first-order approach considering that calving of the aerial part of the glacier occurs when a surface crevasse reaches the sea-level. This criterion is supported by two observations. Firstly, Motyka (1997) showed that calving of the aerial part occurs when the crevasse reaches the sea level, usually followed by the calving of the subaqueous part. Secondly, a surface crevasse reaching the sea-level may be filled with water, if a free connection exists with the sea (Benn et al., 2007b), and is therefore able to propagate downward. Indeed, the water adds a supplementary force $\rho_w g d_w$, where d_w represents the height of water in the crevasse, equal to the height between the sea level and the crack tip. This supplementary hydrostatic pressure, added to the tensile opening stress, counterbalances the cryostatic pressure and/or the ocean water back pressure. Consequently, the opening full stress S_{xx} dominates the force balance and one expects the crevasse to propagates downward. We performed the calculation of K_I in the case where a crevasse reaching the sea level is filled with water. The resulting stress intensity factor becomes positive (from one kilometer upstream to the front) over the whole thickness of the glacier, thus supporting Benn's criterion. This parametrization was successfully applied by Nick et al. (2010) on an idealized geometry, and we choose to prescribe the same criterion. Thereby, the stress intensity factor is computed at a depth d_f equals to the sea level. If $K_\mathrm{I}|_{d_\mathrm{f}} \geq K_\mathrm{Ia}$, the calving occurs.

This framework has two consequences. Firstly, the stress profile $\sigma_{x'x'}$ used to calculate $K_\mathrm{I}|_{d_\mathrm{f}}$ for the arrest criterion is estimated before the propagation of the crevasse. This propagation modifies $\sigma_{x'x'}$, but this effect is not considered here. Secondly, if the condition $K_\mathrm{I}|_d \geq K_\mathrm{Ic}$ is fulfilled but not $K_\mathrm{I}|_{d_\mathrm{f}} \geq K_\mathrm{Ia}$, nothing happens in the model whereas one would expect some brittle crevasse propagation down to d_f to occur. In other words, our model considers LEFM to describe calving but not to simulate crevasse propagation upstream the calving front.

The calving model described in the previous sections is summarized in Fig. 4.

The CDM and LEFM models have been implemented in the finite element ice sheet/ice flow model Elmer/Ice. More information regarding Elmer/Ice can be found in Gagliardini et al. (2013b).

3 A case study

We choose to confront and constrain the previously detailed model of calving against the evolution of Helheim Glacier, a fast-flowing outlet glacier located on the south-east coast of the Greenland ice sheet. We further limit the application and only consider a two-dimensional flow-line problem.

3.1 Data sources

As stated by Andresen et al. (2011), Helheim glacier's front position remained within an extent of 8 km over the last 80 years. These decades have been punctuated by several episodes of glacier advance and retreat. In particular, Helheim underwent a strong retreat between 2001 and 2005, before creating a floating tongue which readvanced beetwen 2005 and 2006 (Howat et al., 2007) and it has been intensively surveyed and studied during the last decade (Luckman et al., 2006; Joughin et al., 2008b; Nick et al., 2009; Bevan et al., 2012; Cook, 2012; Bassis and Jacobs, 2013). It constitutes therefore an interesting case of study to validate a calving model.

As we focus on the front evolution and the calving representation, we only need a bedrock topography covering the last kilometers, in the vicinity of the front. For this reason, we choose to follow the work of Nick et al. (2009) by using their dataset, in which the last 15 km of the glacier are well represented. In this dataset, the initial front position corresponds to the May 2001 pre-collapse geometry. In addition, we choose to consider the glacier as isothermal over its terminating part, by prescribing a constant temperature of $-4.6\,^{\circ}$C, following Nick et al. (2009) again. The constant surface mass balance a_s is taken from Cook (2012) who fitted direct observations from stakes placed over the glacier between 2007 and 2008, which are assumed to represent the annual surface mass balance.

TCD
8, 1631–1671, 2014

3.2 Flowline specificities and numerics

Following our notation system, the ice flows along the horizontal Ox direction and perpendicular to a vertical Oz axis.

The geometry covers the last 30 km of the glacier, with an average thickness varying between 900 m at the inlet boundary, and 700 m at the front. Using the metric from Nick et al. (2009), the beginning of the mesh is located at kilometer 319, and the front at kilometer 347 (see Fig. 5). This geometry is discretized through a structured mesh of 4900 quadrilateral elements, refined on the upper surface and at the front. The size of the elements varies from 300 m to 50 m at the front in the horizontal direction, and from 50 m to 5 m on the upper surface in the vertical direction. Sensitivity tests have been carried out to optimize mesh size: by enhancing the number of element to 15 000, the general behaviour of the model remains unchanged (not shown). The most important criterion to be considered is the element size in the vicinity of the upper surface to allow both damage development and fracture initiation. The final refinement fulfill the need for a proper damage advection (and thus avoiding mesh dependency) and an efficient serial computation. We employed an Arbitrary Lagrangian Eulerian (ALE) method to take into account ice advection and mesh deformation.

The specific boundary conditions adopted for the 2-D application are precised below, otherwise the boundary conditions are those presented in Sect. 2.1.2:

The basal friction C is inferred from the surface velocity data for year 2001 presented in Howat et al. (2007).

In order to represent melting at the calving front, we prescribe an ablation function, linearly increasing with depth, with a zero value at sea level. This constant melting parametrization of 1 m day^{-1} is inspired from the work of Rignot et al. (2010) on four West Greenland glaciers.

The inflow boundary condition ($x = 319$ km) does not correspond to an ice divide. As we consider only the last kilometers before terminus, we made the assumption that the velocity of ice is constant over depth at the upstream boundary, and we impose a Dirichlet condition corresponding to a constant horizontal velocity $u_x = 4000\,\mathrm{m\,a^{-1}}$, in agreement with the observed surface velocity from Howat et al. (2007).

When dealing with a 2-D flowline representation of the flow, we have to take into account some three-dimensional aspects. Especially, lateral friction along the rocky-margins of the glacier can play a significant role, by adding a resistive stress to the flow. Here, it is prescribed through a modified gravity force using a lateral friction coefficient k, as proposed by Gagliardini et al. (2010). This coefficient, which reads:

$$k = \frac{(n+1)^{1/n}}{W^{\frac{n+1}{n}}(2A)^{1/n}} \tag{17}$$

highly depends on the Glen's flow law parameters A and n, as well as on the channel width W (taken from Nick et al., 2009).

Even if the velocity and the surface topography are known and correspond to the observed state of the glacier in May 2001, some adjustments must be made in order to obtain a stable steady state, before running sensitivity tests (Gillet-Chaulet et al., 2012). We let the geometry adjust to the prescribed boundary conditions and inversed basal friction for approximately 8 years.

3.3 Results and discussion

3.3.1 Calibration of the model: sampling strategy

As mentioned in the previous sections, the acceptable ranges for three parameters σ_{th}, B, and D_{c} have to be evaluated. This is obtained thanks to a latin hypercube sampling. This methods requires a number of variables to be tested, and a number of simulations. As the exact values for our parameters are unknown, theses are randomly sampled between given ranges. The stress threshold σ_{th} is estimated to be within the range of $[0.02, 0.2]$ MPa. The lower bound is near to the one given in Pralong and Funk (2005). If $\sigma_{\mathrm{th}} > 0.2$, the stress field is not high enough to reach the damage thresh-

TCD
8, 1631–1671, 2014

old, and damaging never happens. The Damage enhancement factor B is related to the rate at which the damage increases, once the damage criterion χ is positive. This value is particularly difficult to evaluate, especially because it does not lay on laboratory experiments or observations. Thus, we choose a large range $[0.5,3]$. However, one must note that this parameter should have a value which keeps the stress field in the vicinity of the damage envelope, once the stress has been released by damaging. The critical damage value D_c has already been documented (Pralong and Funk, 2005; Borstad et al., 2012; Duddu and Waisman, 2013). According to their values, we set our range within $[0.4,0.6]$. The number of computed simulations was 250.

3.3.2 Calibration of the model: spin-up

Damage can be produced anywhere in the glacier. As we need to obtain a steady state for the damage field, it is necessary to let the damage created upstream be advected to the front. This spin-up lasts 8 years. During this period, the front is maintained at its initial position, without submarine frontal melting, and the procedure of calving is not activated. Once the steady state is obtained, the front is released, the frontal melting is prescribed and the calving procedure is activated.

3.3.3 Model response

As mentioned in Andresen et al. (2011), over the last century, Helheim Glacier has probably undergone several advance and retreat cycles, and observations of sand deposits imply a variation of the terminus around less than 10 km. The knowledge about the potential triggering mechanisms for retreat cycles is still poor: according to Joughin et al. (2008b) and Andresen et al. (2011), this retreat may have been forced by an enhanced summer temperature, and higher ocean water temperature, although sensitivity of calving to temperature remains unclear.

For these reasons, we did not try to reproduce the precise chronology of the Helheim's recent retreat in this paper. Instead, we study the dynamical behaviour of the model with respect to the different sets of parameters, and try to distinguish between unrealistic and realistic behaviours. The simulations presented in the previous sections were run during 4 years after the spin-up. Among the 250 sets of parameters, the model response can be split in 3 classes, illustrated in Fig. 6. The blue curve on this figure represents a case where the calving almost never happened, and where the glacier advances too much, creating a floating tongue of several kilometers. The yellow curve illustrates a case where the calving occurs too quickly, leading to a front retreat far upstream. The red curve represents a case consistent against observations, where the front of the glacier is punctuated by irregular calving events, forcing the glacier to keep its extent in an acceptable range of values.

This classification in three classes of behaviour can be generalized to the 250 simulations. In order to eliminate aberrant behaviour, we prescribe a sanity-check, by considering plausible sets of parameters as the ones which lead to a simulated front position within the range [340 km, 350 km]. The results are represented in Fig. 7, in the space of parameter (B, $\overline{\sigma_{\mathrm{th}}}$). On this figure, we distinguished once again the same three classes, blue plus signs, yellow crosses and red diamonds, representing respectively the case where the front exceeds 350 km, the case where the front retreats more inland than 340 km, and the case where the front remains within this range. The curves illustrated in Fig. 6 are represented here by closed circles using the same colorscale.

The steadily advance of the front without or with few calving events can be explained considering the couple (B, $\overline{\sigma_{\mathrm{th}}}$). These simulations are characterized by a low value of B and/or a high value of $\overline{\sigma_{\mathrm{th}}}$. This means that either the incrementation of damage is too low, or the stress threshold is too high to allow damage initiation. In these cases, damage production is not sufficient to reach the calving criterion $D = D_{\mathrm{c}}$, whatever its chosen value. In addition, when $\overline{\sigma_{\mathrm{th}}}$ is too high, the damage may only increases in the area where the traction is very high, meaning at the top of bumps, in the immediate vicinity of the surface. As a consequence, the damage does never reach a sufficient depth to trigger calving.

On the contrary, the too fast retreat of the front can be explained as follows: when B is high and/or $\overline{\sigma_{th}}$ is low, the initiation of damage is easy, and the increment is important, leading to a high value of damage at the surface of the glacier. As a consequence, the criterion $D > D_c$ is easily reached, leading to a too rapid sequence of calving events.

One must note that in some cases where the retreat of the front was too important, the simulations stopped before reaching the inlet boundary. Due to the over deepening, the front retreated quickly in an area where the height of ice a.s.l. was much more important than the one observed in reality. Consequently, the model was unable to deal with the large velocity of ice and mesh deformation, and so degenerated. However, this behaviour agrees our sanity check, as the lower bound is anyway exceeded.

Nevertheless, the discretization into three classes of parameter should not hide the fact that there is a continuum in the behavior of the glacier, depending on the value of $(\overline{\sigma_{th}}, B, D_c)$, and the boundaries between classes are not abrupt. Thus, simulations may present some front position out of the range [340 km, 350 km] (and then considered as unrealistic), but still have a general dynamics which is not far from realistic behaviours.

3.3.4 Realistic behaviour analysis

The acceptable class of parameters is the one describing the diagonal in Fig. 7. During these simulations, the front remained between the two limits and has a consistent behaviour when compared to observations. The simulation corresponding to the set of parameters ($\overline{\sigma_{th}} = 0.072$ MPa, $B = 1.870$ MPa^{-1}, and $D_c = 0.529$) represented as the red circle on Fig. 7 can be seen as an example of consistent behaviour. The Helheim's front remains in the range defined by our sanity check (i.e. [340 km, 350 km]). As represented on Fig. 8a and b, damage increases in the area where the traction is high enough to exceed $\overline{\sigma_{th}}$, that is over the bumps. This is consistent with observations of glaciers flowing over slope ruptures (Pralong and Funk, 2005). Here, the value of $\overline{\sigma_{th}}$ is low enough, and the damage develops over a depth of almost 15 m, at a rate high enough to reach the critical damage value D_c at the front and initiate calving (see Fig. 8c and d).

Mottram and Benn (2009) investigated crevasse depth in the vicinity of the terminus of a Svalbard tidewater calving glacier, and showed that most of crevasses were under 10 m depth. In our experiments, damage develops at depths around 5 m to 15 m when calving usually occurs. As described previously, this value of d must be large enough to account for critical crevasse propagation, and is consistent with observations.

The parameter D_c is a control on whether the fracture propagates or not. If it is low, the conditions for crevasse propagation may occur easily, as soon as the criterion on LEFM is fulfilled. On the contrary, if D_c is too high, damage may never reach a sufficient depth to initiate fracture propagation. As a consequence, the value of D_c controls the location of the calving front. However, D_c is tightly linked with (B, $\overline{\sigma_{th}}$) through the production of damage upstream and it must be chosen in the same range as the level of damage at the front.

After the sensitivity to the three main numerical parameters $\overline{\sigma_{th}}$, B, and D_c has been realized, the influence of other parameters discussed above has been undertaken. Results showed that the model is only slightly sensitive to the parameter K_{Ic}. As ice toughness increases, it becomes more and more difficult to initiate fracture propagation. However, changing the value of ice toughness does not change the general behaviour of the system (not shown). Varying α does not have a significant impact. Indeed, the computation of the arrest criterion is realized at depth equals to the sea level. At this depth, the stress intensity factor is larger than the ice toughness (not shown), and thus, higher than K_{Ia}, whatever the value of α.

At last, the sensitivity to the initial heterogeneous micro-defects distribution introduced in Sect. 2.2.1 has been tested. The standard deviation of the distribution of stress threshold $\frac{\delta\sigma_{th}}{\overline{\sigma_{th}}}$ was varied within the range [0.005; 0.2]. Results show that the consistency of the behavior remains unchanged, but the spatial and temporal variability of the front position is modified (not shown). A higher standard deviation leads to a higher variability in the front position. In addition, we investigated the natural variability of the model. Repeating simulations with the same $\delta\sigma_{th}$ but different realizations of the local disorder does not change the general behaviour of the model. However, it modifies both the temporal and spatial distribution of calving events (not shown). These results highlight the existence of an intrinsic variability of the glacier dynamics.

According to our sanity check, among the 250 simulations, 59 presents a realistic behaviour. These experiments totalize 5508 calving events. The distribution of front retreats is given in Fig. 9. This figure shows the probability of realization of a calving event smaller than a given value (x axis), for the real distribution (blue crosses), and for the corresponding gaussian distribution (dashed-red curve). The flattening of the blue curve for calving events larger than 300 m (compared to the red curve) illustrates the fact that our model produces a higher number of large events than it should be if following a gaussian distribution. On the contrary, the steepening of the blue curve for the smaller events (< 125 m) indicates a deficit of small events compared to gaussian statistics. This deficit may be related to the mesh-size, as the size of events approaches the size of the mesh refinement at the front. This possible mesh-effect is not relevant for large calving events. Therefore, our results show the emergence of two population of calving event sizes from internal glacier dynamics: between 100 m and 300 m, the distribution is essentially gaussian, whereas a population of anomalously large events is observed above 400 m. This distinction is also qualitatively visible on Fig. 6. Finally, it is important to note that this plot should not be interpreted as an icebergs size distribution. Indeed, one must distinguish between the front retreat and the size of resulting iceberg(s), which may be strongly different, as the calved portion of ice can fragment into many icebergs and/or capsize. However, distribution of the distance of front retreat may remain an interesting parameter to validate the model, but it would require a continuous tracking of the front position of the actual glacier, as discrete determination of the position (Joughin et al., 2008b) may bias the estimation of the retreat of single events, particularly for the small sizes population. We are not aware of the existence of such a dataset existing on Helheim glacier.

Obviously, in the experiments presented in this paper, the cycles of advance and retreat which can be observed on Fig. 6 are not related to any variability in the external forcing, but results from the dynamics of the glacier only. This brings us to the conclusion that a variation of the front position of several kilometers may be related to the glacier internal dynamics and are not necessarily the consequence of an external forcing.

4 Conclusions

In this work, we combined continuum damage mechanics and linear elastic fracture mechanics to propose a physically-based calving model able (i) to reproduce the slow development of small fractures leading to the apparition of macroscopic crevasse fields, over long timescales, while considering ice as a viscous material, and (ii) to deal with the elastic behaviour of breaking ice, consistent with the critical crevasse propagation triggering calving events, characterized by very short timescales. The model has been applied to Helheim Glacier, which allowed to constrain the acceptable sets of parameters. In this case, the front was dynamically maintained within the same extent as the one observed during the last century.

We showed that the ability of the model to have a realistic behaviour lays on a balance between the three damage parameters ($\overline{\sigma_{\mathrm{th}}}$, B, and D_c). The first two parameters must be in a range which allows the damage to develop sufficiently in the damaging areas before being transported downstream. Then, the maximal value of damage reaching the front should be close to D_c and at a sufficient depth in order to trigger calving.

One must keep in mind that this sensitivity test is based on the response of one specific glacier to a poorly known external forcing and with limited observations. In these conditions, we show that some sets of parameters definitely generate a reliable behaviour, but one should be careful when considering another configuration, and make sure that the response of the model is realistic. Despite this limitation, this calving model based on realistic physical approaches gives reliable results and could be easily implemented in classical ice-flow finite element models.

The calving process described in this paper is immediately driven by the variation in longitudinal stretching associated with horizontal velocity gradients, producing a first-order control on calving rate, as stated by Benn et al. (2007b). Local aspects, involving undercutting or force imbalance at ice cliffs are described as second-order calving processes. Using this model, further work could be undertaken in enhancing the general knowledge of these second-order phenomena.

Appendix A

Weight function for stress intensity factor

As stated by Glinka (1996), the weight function for the computation of the stress intensity factor depends on the specific geometry of the initial crack. For an edge crack in a finite width plate, the weight function is given by:

$$\beta(y,d) = \frac{2}{\sqrt{2\pi(d-y)}}\left[1 + M_1\left(1-\frac{y}{d}\right)^{1/2} + M_2\left(1-\frac{y}{d}\right)^{1} + M_3\left(1-\frac{y}{d}\right)^{3/2}\right]$$

The weight function depends on 3 numerical parameters, polynomial functions of the ratio d/H. They read:

$$\begin{aligned} M_1 = {} & 0.0719768 - 1.513476\left(\frac{d}{H}\right) - 61.1001\left(\frac{d}{H}\right)^2 + 1554.95\left(\frac{d}{H}\right)^3 \\ & - 14\,583.8\left(\frac{d}{H}\right)^4 + 71\,590.7\left(\frac{d}{H}\right)^5 - 205\,384\left(\frac{d}{H}\right)^6 + 356\,469\left(\frac{d}{H}\right)^7 \\ & - 368\,270\left(\frac{d}{H}\right)^8 + 208\,233\left(\frac{d}{H}\right)^9 - 49\,544\left(\frac{d}{H}\right)^{10} \end{aligned}$$

$$M_2 = 0.246984 + 6.47583\left(\frac{d}{H}\right) + 176.456\left(\frac{d}{H}\right)^2 - 4058.76\left(\frac{d}{H}\right)^3 + 37\,303.8\left(\frac{d}{H}\right)^4 - 181\,755\left(\frac{d}{H}\right)^5 + 520\,551\left(\frac{d}{H}\right)^6 - 904\,370\left(\frac{d}{H}\right)^7 + 936\,863\left(\frac{d}{H}\right)^8 - 531\,940\left(\frac{d}{H}\right)^9 + 127\,291\left(\frac{d}{H}\right)^{10}$$

$$M_3 = 0.529659 - 22.3235\left(\frac{d}{H}\right) + 532.074\left(\frac{d}{H}\right)^2 - 5479.53\left(\frac{d}{H}\right)^3 + 28\,592.2\left(\frac{d}{H}\right)^4 - 81\,388.6\left(\frac{d}{H}\right)^5 + 128\,746\left(\frac{d}{H}\right)^6 - 106\,246\left(\frac{d}{H}\right)^7 + 35\,780.7\left(\frac{d}{H}\right)^8$$

Acknowledgements. This study was funded by the Agence Nationale pour la Recherche (ANR) through the SUMER, Blanc SIMI 6-2012. We acknowledge the use of data and/or data products from CReSIS generated with support from NSF grant ANT-0424589 and NASA grant NNX10AT68G. We further thank the CSC-IT Center for Science Ltd (Finland) for their support in Elmer/Ice development and Joe Todd for developments on mesh deformations.

References

Albrecht, T. and Levermann, A.: Fracture field for large-scale ice dynamics, J. Glaciol., 58, 165–177, 2012. 1639

Andresen, C. S., Straneo, F., Ribergaard, M. H., Bjørk, A. A., Andersen, T. J., Kuijpers, A., Nørgaard-Pedersen, N., Kjær, K. H., Schjøth, F., Weckström, K., and Ahlström, A. P.: Rapid response of Helheim Glacier in Greenland to climate variability over the past century, Nat. Geosci., 5, 37–41, 2011. 1646, 1649

Åström, J. A., Riikilä, T. I., Tallinen, T., Zwinger, T., Benn, D., Moore, J. C., and Timonen, J.: A particle based simulation model for glacier dynamics, The Cryosphere, 7, 1591–1602, doi:10.5194/tc-7-1591-2013, 2013. 1633

Bassis, J. and Jacobs, S.: Diverse calving patterns linked to glacier geometry, Nat. Geosci., 6, 833–836, 2013. 1633, 1646

Benn, D. I., Hulton, N. R., and Mottram, R. H.: "Calving laws", "sliding laws" and the stability of tidewater glaciers, Ann. Glaciol., 46, 123–130, 2007a. 1644

Benn, D. I., Warren, C. R., and Mottram, R. H.: Calving processes and the dynamics of calving glaciers, Earth-Sci. Rev., 82, 143–179, 2007b. 1640, 1645, 1655

Bevan, S. L., Luckman, A. J., and Murray, T.: Glacier dynamics over the last quarter of a century at Helheim, Kangerdlugssuaq and 14 other major Greenland outlet glaciers, The Cryosphere, 6, 923–937, doi:10.5194/tc-6-923-2012, 2012. 1646

Borstad, C. P., Khazendar, A., Larour, E., Morlighem, M., Rignot, E., Schodlok, M. P., and Seroussi, H.: A damage mechanics assessment of the Larsen B ice shelf prior to collapse: Toward a physically-based calving law, Geophys. Res. Lett., 39, L18502, doi:10.1029/2012GL053317, 2012. 1633, 1637, 1641, 1649

Cook, S. J.: Environmental Controls on Calving in Grounded Tidewater Glaciers, Ph.D. thesis, Swansea University, Swansea, UK, 2012. 1646

Depoorter, M., Bamber, J., Griggs, J., Lenaerts, J., Ligtenberg, S., van den Broeke, M., and Moholdt, G.: Calving fluxes and basal melt rates of Antarctic ice shelves, Nature, 502, 82–92, 2013. 1632

Duddu, R. and Waisman, H.: A temperature dependent creep damage model for polycrystalline ice, Mech. Mater., 46, 23–41, 2012. 1639

Duddu, R. and Waisman, H.: A nonlocal continuum damage mechanics approach to simulation of creep fracture in ice sheets, Comput. Mech., 51, 1–14, 2013. 1633, 1639, 1649

Durand, G., Gagliardini, O., De Fleurian, B., Zwinger, T., and Le Meur, E.: Marine ice sheet dynamics: hysteresis and neutral equilibrium, J. Geophys. Res.-Earth, 114, F03009, doi:10.1029/2008JF001170, 2009. 1636

Favier, L., Gagliardini, O., Durand, G., and Zwinger, T.: A three-dimensional full Stokes model of the grounding line dynamics: effect of a pinning point beneath the ice shelf, The Cryosphere, 6, 101–112, doi:10.5194/tc-6-101-2012, 2012. 1636

Fischer, M., Alley, R., and Engelder, T.: Fracture toughness of ice and firn determined from the modified ring test, J. Glaciol., 41, 383–394, 1995. 1643

Gagliardini, O., Durand, G., Zwinger, T., Hindmarsh, R., and Le Meur, E.: Coupling of ice-shelf melting and buttressing is a key process in ice-sheets dynamics, Geophys. Res. Lett., 37, L14501, doi:10.1029/2010GL043334, 2010. 1632, 1648

Gagliardini, O., Weiss, J., Duval, P., and Montagnat, M.: On Duddu and Waisman (2012a, b) concerning continuum damage mechanics applied to crevassing and icebergs calving, J. Glaciol., 59, 797–798, 2013a. 1639

Heinke, J., Ostberg, S., Schaphoff, S., Frieler, K., Müller, C., Gerten, D., Meinshausen, M., and Lucht, W.: A new climate dataset for systematic assessments of climate change impacts as a function of global warming, Geosci. Model Dev., 6, 1689–1703, doi:10.5194/gmd-6-1689-2013, 2013b. 1645

Gillet-Chaulet, F., Gagliardini, O., Seddik, H., Nodet, M., Durand, G., Ritz, C., Zwinger, T., Greve, R., and Vaughan, D. G.: Greenland ice sheet contribution to sea-level rise from a new-generation ice-sheet model, The Cryosphere, 6, 1561–1576, doi:10.5194/tc-6-1561-2012, 2012. 1648

Glinka, G.: Development of weight functions and computer integration procedures for calculating stress intensity factors around cracks subjected to complex stress fields, Stress and Fatigue-Fracture Design, Petersburg Ontario, Canada, Progress Report, 1, 1, 1996. 1643, 1655

Hayhurst, D.: Creep rupture under multi-axial states of stress, J. Mech. Phys. Solids, 20, 381–382, 1972. 1639

Howat, I. M., Joughin, I., and Scambos, T. A.: Rapid changes in ice discharge from Greenland outlet glaciers, Science, 315, 1559–1561, 2007. 1646, 1647, 1648

Jay-Allemand, M., Gillet-Chaulet, F., Gagliardini, O., and Nodet, M.: Investigating changes in basal conditions of Variegated Glacier prior to and during its 1982–1983 surge, The Cryosphere, 5, 659–672, doi:10.5194/tc-5-659-2011, 2011. 1636

Joughin, I., Das, S. B., King, M. A., Smith, B. E., Howat, I. M., and Moon, T.: Seasonal speedup along the western flank of the Greenland Ice Sheet, Science, 320, 781–783, 2008a. 1633

Joughin, I., Howat, I., Alley, R. B., Ekstrom, G., Fahnestock, M., Moon, T., Nettles, M., Truffer, M., and Tsai, V. C.: Ice-front variation and tidewater behavior on Helheim and Kangerdlugssuaq Glaciers, Greenland, J. Geophys. Res.-Earth, 113, F01004, doi:10.1029/2007JF000837, 2008b. 1646, 1649, 1653

TCD
8, 1631–1671, 2014

Jouvet, G., Picasso, M., Rappaz, J., Huss, M., and Funk, M.: Modelling and Numerical Simulation of the Dynamics of Glaciers Including Local Damage Effects, Mathematical Modelling of Natural Phenomena, 6, 263–280, 2011. 1637

Kachanov, L.: Time of the rupture process under creep conditions, Isv. Akad. Nauk. SS R. Otd Tekh. Nauk, 8, 26–31, 1958. 1633, 1637

Labbens, R., Pellissier-Tanon, A., and Heliot, J.: Application de la théorie linéaire de la mécanique de la rupture aux structures métalliques épaisses – Méthodes pratiques de calcul des facteurs d'intensité de contrainte, Rev. Phys. Appl., 9, 587–598, 1974. 1642, 1643

Lemaitre, J., Chaboche, J., and Germain, P.: Mécanique des Matériaux Solides, vol. 7, Dunod, Paris, 1988. 1637, 1638

Luckman, A., Murray, T., De Lange, R., and Hanna, E.: Rapid and synchronous ice-dynamic changes in East Greenland, Geophys. Res. Lett., 33, L03503, doi:10.1029/2005GL025428, 2006. 1646

Ma, Y., Gagliardini, O., Ritz, C., Gillet-Chaulet, F., Durand, G., and Montagnat, M.: Enhancement factors for grounded ice and ice shelves inferred from an anisotropic ice-flow model, J. Glaciol., 56, 805–812, 2010. 1635

Mottram, R. H. and Benn, D. I.: Testing crevasse-depth models: a field study at Breioamerkurjokull, Iceland, J. Glaciol., 55, 746–752, 2009. 1633, 1641, 1652

Motyka, R.: Deep-water calving at Le Conte Glacier, southeast Alaska, Byrd Polar Res. Cent. Rep., 15, 115–118, 1997. 1644

Murakami, S. and Ohno, N.: A continuum theory of creep and creep damage, in: Creep in Structures, Springer, Tempaku-cho, Toyohashi 440, Japan, 422–444, 1981. 1638

Nath, P. and Vaughan, D.: Subsurface crevasse formation in glaciers and ice sheets, J. Geophys. Res.-Sol. Ea., 108, 2020, 2003. 1641

Nick, F. M., Vieli, A., Howat, I. M., and Joughin, I.: Large-scale changes in Greenland outlet glacier dynamics triggered at the terminus, Nat. Geosci., 2, 110–114, 2009. 1646, 1647, 1648

Nick, F. M., van der Veen, C. J., Vieli, A., and Benn, D. I.: A physically based calving model applied to marine outlet glaciers and implications for the glacier dynamics, J. Glaciol., 56, 781–794, 2010. 1633, 1645

Nick, F. M., Vieli, A., Andersen, M. L., Joughin, I., Payne, A., Edwards, T. L., Pattyn, F., and van de Wal, R. S.: Future sea-level rise from Greenland's main outlet glaciers in a warming climate, Nature, 497, 235–238, 2013. 1633

TCD
8, 1631–1671, 2014

Nye, J.: The distribution of stress and velocity in glaciers and ice-sheets, P. Roy. Soc. Lond A Mat., 239, 113–133, 1957. 1633

Otero, J., Navarro, F. J., Martin, C., Cuadrado, M. L., and Corcuera, M. I.: A three-dimensional calving model: numerical experiments on Johnsons Glacier, Livingston Island, Antarctica, J. Glaciol., 56, 200–214, 2010. 1633

Pralong, A. and Funk, M.: Dynamic damage model of crevasse opening and application to glacier calving, J. Geophys. Res., 110, B01309, doi:10.1029/2004JB003104, 2005. 1633, 1637, 1638, 1639, 1640, 1648, 1649, 1651

Pralong, A., Funk, M., and Lüthi, M. P.: A description of crevasse formation using continuum damage mechanics, Ann. Glaciol., 37, 77–82, 2003. 1633, 1637, 1640

Ravi-Chandar, K. and Knauss, W.: An experimental investigation into dynamic fracture: I. Crack initiation and arrest, Int. J. Fracture, 25, 247–262, 1984. 1644

Rignot, E. and Kanagaratnam, P.: Changes in the velocity structure of the Greenland Ice Sheet, Science, 311, 986–990, 2006. 1632

Rignot, E., Koppes, M., and Velicogna, I.: Rapid submarine melting of the calving faces of West Greenland glaciers, Nat. Geosci., 3, 187–191, 2010. 1632, 1647

Rist, M. A., Sammonds, P. R., Murrell, S. A. F., Meredith, P. G., Oerter, H., and Doake, C. S. M.: Experimental fracture and mechanical properties of Antarctic ice preliminary results, Ann. Glaciol., 23, 284–292, 1996. 1643

Rist, M. A., Sammonds, P. R., Murrell, S. A. F., Meredith, P. G., Doake, C. S. M., Oerter, H., and Matsuki, K.: Experimental and theoretical fracture mechanics applied to Antarctic ice fracture and surface crevassing, J. Geophys. Res., 104, 2973–2987, 1999. 1638, 1641

Scambos, T. A., Bohlander, J., Shuman, C., and Skvarca, P.: Glacier acceleration and thinning after ice shelf collapse in the Larsen B embayment, Antarctica, Geophys. Res. Lett., 31, L18402, doi:10.1029/2004GL020670, 2004. 1632

Schulson, E. M. and Duval, P.: Creep and Fracture of Ice, Cambridge University Press Cambridge, Cambridge, 2009. 1643

Shepherd, A., Ivins, E. R., Geruo, A., Barletta, V. R., Bentley, M. J., Bettadpur, S., Briggs, K. H., Bromwich, D. H., Forsberg, R., Galin, N., Horwath, M., Jacobs, S., Joughin, I., King, M. A., Lenaerts, J. T. M., Li, J., Ligtenberg, S. R. M., Luckman, A., Luthcke, S. B., McMillan, M., Meister, R., Milne, G., Mouginot, J., Muir, A., Nicolas, J. P., Paden, J., Payne, A. J., Pritchard, H., Rignot, E., Rott, H., Sandberg Sørensen, L., Scambos, T. A., Scheuchl, B., Schrama, E. J. O., Smith, B., Sundal, A. V., van Angelen, J. H., van de Berg, W. J., van den

TCD
8, 1631–1671, 2014

Title Page
Abstract | Introduction
Conclusions | References
Tables | Figures
◀| |▶
◀ ▶
Back | Close
Full Screen / Esc
Printer-friendly Version
Interactive Discussion

Broeke, M. R., Vaughan, D. G., Velicogna, I., Wahr, J., Whitehouse, P. L., Wingham, D. J., Yi, D., Young, D., and Zwally, H. J.: A reconciled estimate of ice-sheet mass balance, Science, 338, 1183–1189, 2012. 1632

Smith, R. A.: The application of fracture mechanics to the problem of crevasse penetration, J. Glaciol., 17, 223–228, 1976. 1641

van der Veen, C.: Fracture mechanics approach to penetration of bottom crevasses on glaciers, Cold Reg. Sci. Technol., 27, 213–223, 1998a. 1633, 1641, 1642, 1644

van der Veen, C.: Fracture mechanics approach to penetration of surface crevasses on glaciers, Cold Reg. Sci. Technol., 27, 31–47, 1998b. 1633, 1641, 1644

Vaughan, D. G.: Relating the occurrence of crevasses to surface strain rates, J. Glaciol., 39, 255–266, 1993. 1639

Weiss, J.: Subcritical crack propagation as a mechanism of crevasse formation and iceberg calving, J. Glaciol., 50, 109–115, 2004. 1641

Weiss, J. and Schulson, E. M.: Coulombic faulting from the grain scale to the geophysical scale: lessons from ice, J. Phys. D, 42, 214017, 2009. 1639

Xiao, J. and Jordaan, I.: Application of damage mechanics to ice failure in compression, Cold Reg. Sci. Technol., 24, 305–322, 1996. 1637

Table 1. Physical and numerical parameters. Tunable parameters are indicated in bold.

Parameter	Symbol	Value	Unit
Fluidity parameter	A		$\mathrm{MPa^{-3}\,a^{-1}}$
Damage enhancement factor	$\boldsymbol{B}$	0.5 to 3	$\mathrm{Pa^{-1}}$
Bed friction parameter	C		$\mathrm{Pa\,m^{-1/3}\,s^{1/3}}$
Crevasse depth	d		m
Water depth inside the crevasse	d_w		m
Damage variable	D	0 to 1	
Critical damage variable	$\boldsymbol{D_c}$	0.4 to 0.6	
Glen's enhancement factor	E	1	
Standard gravity	g	9.81	$\mathrm{m\,s^{-2}}$
Ice Thickness	H		m
Lateral friction coefficient	k		$\mathrm{Pa\,m^{-4/3}\,a^{1/3}}$
Stress intensity factor (Mode I)	K_I		$\mathrm{MPa\,m^{1/2}}$
Fracture toughness (Mode I)	K_Ic	0.2	$\mathrm{MPa\,m^{1/2}}$
Arrest criterion (Mode I)	K_Ia		$\mathrm{MPa\,m^{1/2}}$
Sea level	l_w		m
Bed friction exponent	m	1/3	
Glen exponent	n	3	
Deviatoric Cauchy stress tensor	$\mathbf{S}$		Pa
Effective deviatoric Cauchy stress tensor	$\tilde{\mathbf{S}}$		Pa
Velocity field	u		$\mathrm{m\,s^{-1}}$
Channel width	W		m
Fracture arrest parameter	α	0.5	
Weigth function	β		$\mathrm{m^{-1/2}}$
Strain rate	$\dot{\epsilon}$		
Viscosity	η		$\mathrm{MPa^{-1}\,a}$
Water density	ρ_w	1000	$\mathrm{kg\,m^{-3}}$
Ice density	ρ_I	900	$\mathrm{kg\,m^{-3}}$
Cauchy stress tensor	σ		Pa
Effective Cauchy stress tensor	$\tilde{\sigma}$		Pa
Maximum principal stress	σ_I		Pa
Stress threshold	$\boldsymbol{\sigma_{th}}$	20×10^3 to 200×10^3	Pa

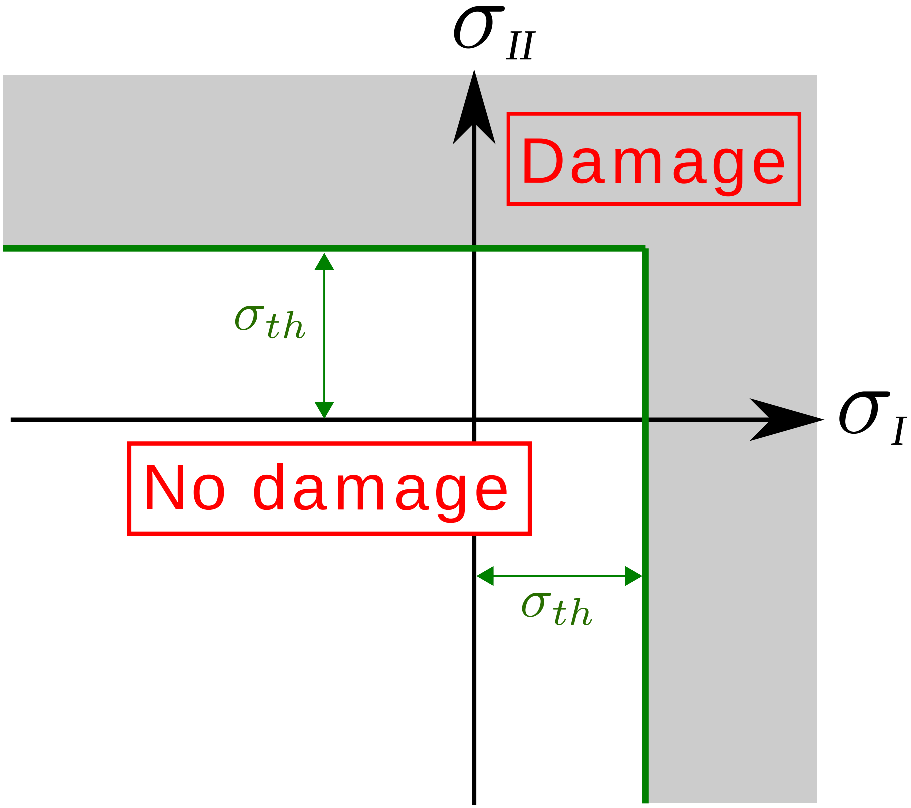

Fig. 1. Damage envelope in the space of principal stresses. σ_I and σ_{II} respectively represent the first principal stress and the second principal stress, and σ_{th} is the stress threshold. The shaded area corresponds to the stress conditions under which damage occurs.

TCD
8, 1631–1671, 2014

Combining damage and fracture mechanics to model calving

J. Krug et al.

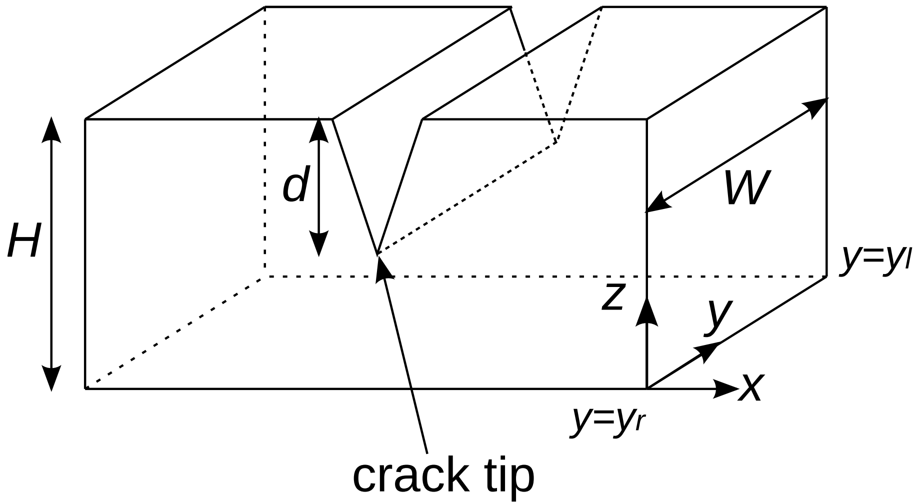

Fig. 2. Crevasse shape. *H* refers to the ice thickness and *d* is the crevasse depth.

TCD
8, 1631–1671, 2014

Combining damage and fracture mechanics to model calving

J. Krug et al.

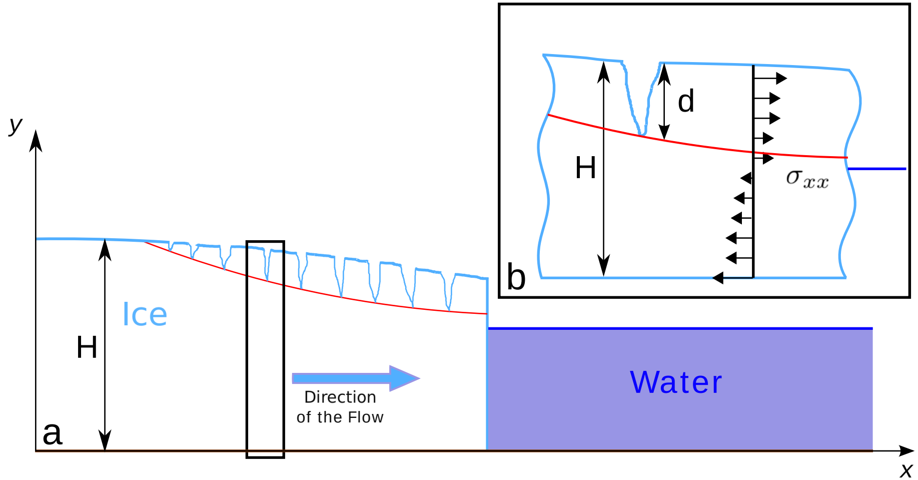

Fig. 3. (a) Shape of a grounded glacier and **(b)** zoom on the black rectangle. The red curve illustrates the contour of critical damage $D = D_c$ for which we compute the along-flow component of the Cauchy stress tensor σ_{xx} multiplied by the weight function and integrated over the crevasse depth d.

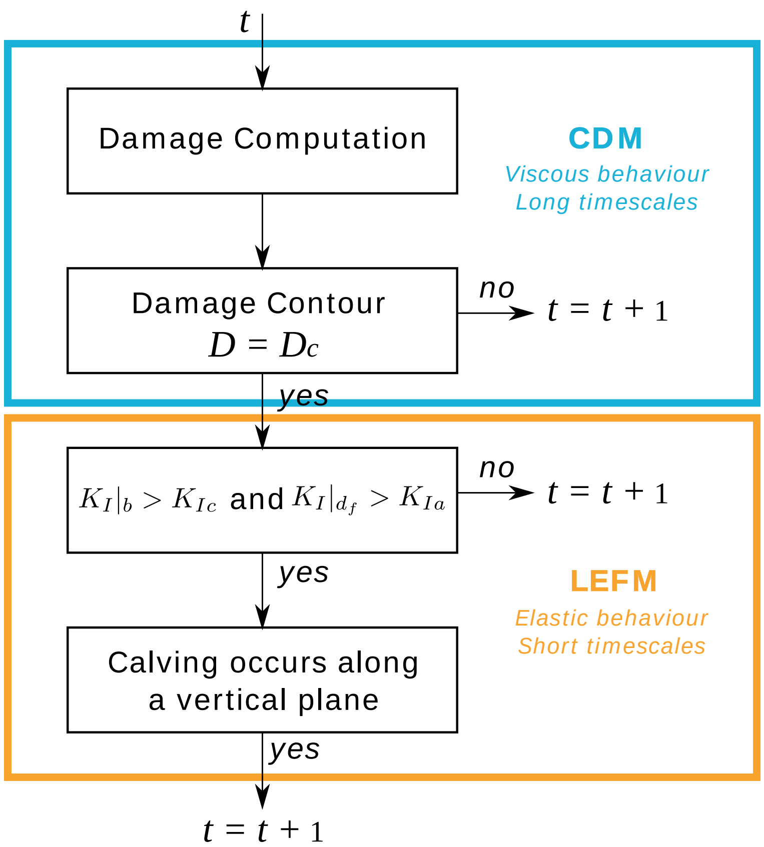

Fig. 4. Algorithm of the calving model where *t* refers to the time step. Blue shape indicates the area of CDM application, where ice undergoes a viscous behaviour and orange shape corresponds to the LEFM domain of application, where ice has an elastic behaviour, representing fracture propagation and calving event.

TCD
8, 1631–1671, 2014

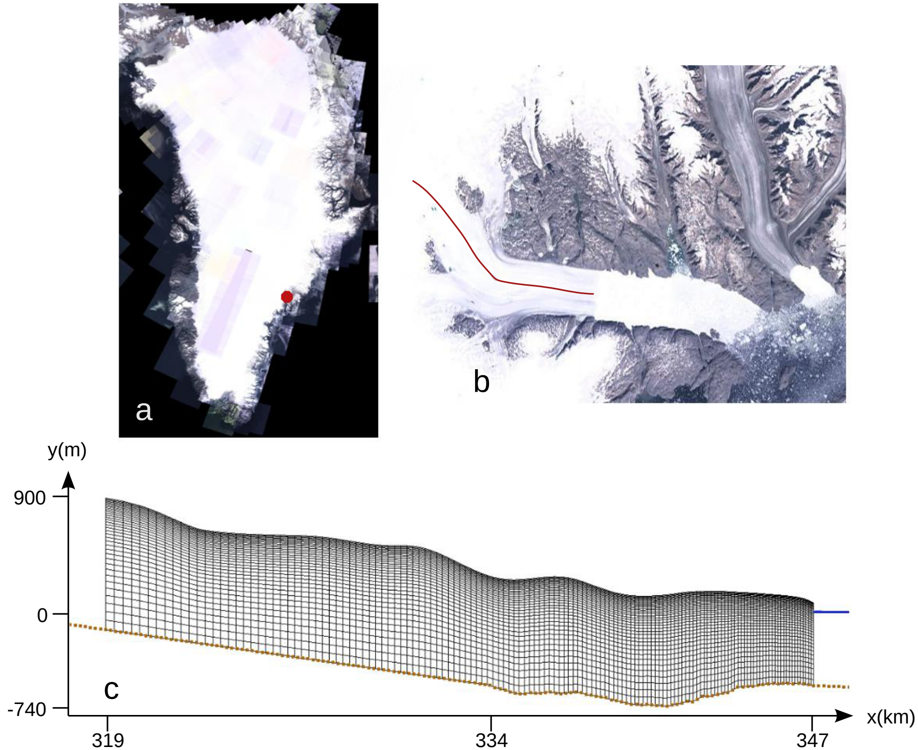

Fig. 5. Glacier location and geometry. **(a)** Location on the Greenland Ice Sheet (red point). **(b)** Zoom on the Helheim terminus and the considered flowline (red curve). **(c)** Mesh extracted from this flowline. The starting position correspond to the front position at 347 km. The blue line represents the sea level.

TCD
8, 1631–1671, 2014

Combining damage and fracture mechanics to model calving

J. Krug et al.

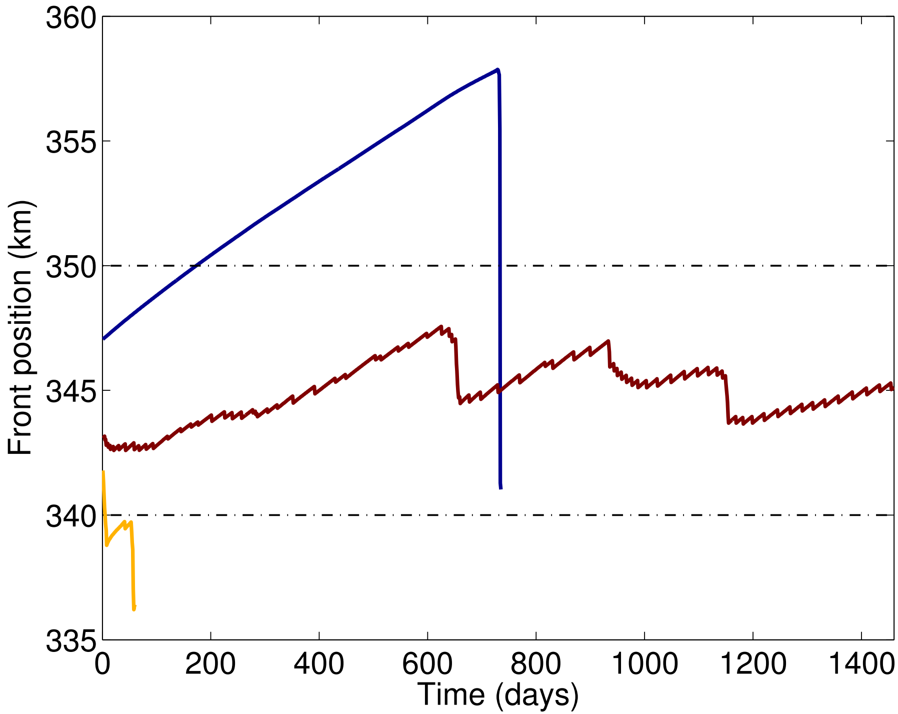

Fig. 6. Position of the calving front as a function of time. Each color correspond to a set of parameter $\overline{\sigma_{th}}$, B, and D_c. The blue color represents an advance with almost no calving ($\overline{\sigma_{th}}$ = 0.180 MPa, B = 0.878 MPa^{-1}, and D_c = 0.460); the yellow one corresponds to a severe retreat ($\overline{\sigma_{th}}$ = 0.088 MPa, B = 2.883 MPa^{-1}, and D_c = 0.427) ; the red one presents a behaviour consistent against observations ($\overline{\sigma_{th}}$ = 0.072 MPa, B = 1.870 MPa^{-1}, and D_c = 0.529). The yellow curve stopped after 60 days because the glacier retreated too far inland. The blue curve stopped after 735 days because the glacier retreat was too large to be supported by the model.

TCD
8, 1631–1671, 2014

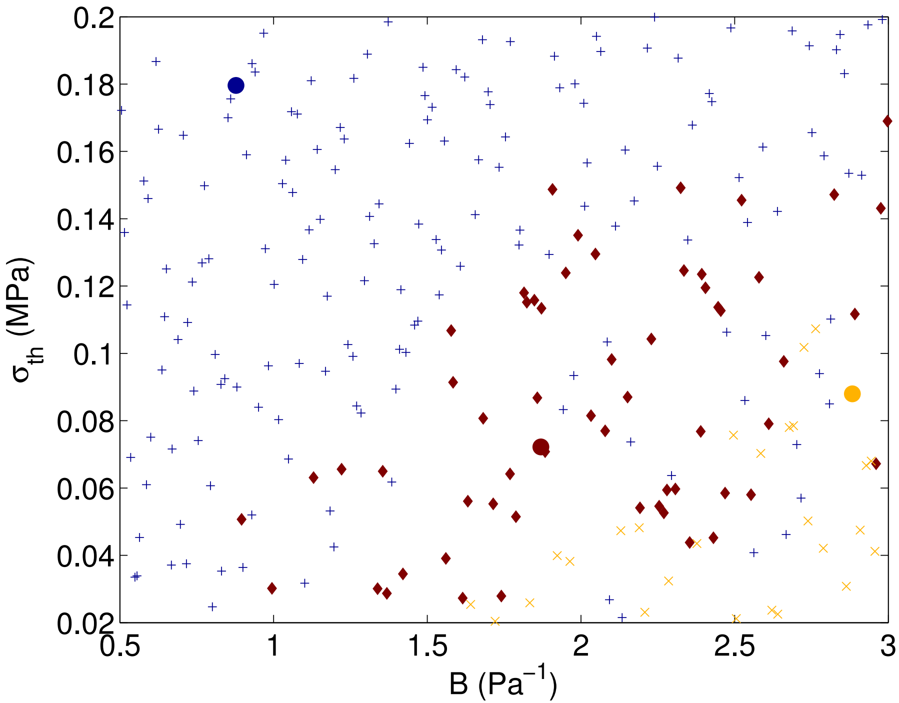

Fig. 7. Sampling in the space of damage parameters B, $\overline{\sigma_{th}}$. Blue plus signs, and yellow crosses respectively represent simulations for which the front exceed 350 km and simulation for which the front retreated below 340 km. Red diamonds represent the successful simulations. Blue, red and yellow circles corresponds to the same colored curves in Fig. 6. Red circle corresponds to the simulation illustrated on Fig. 8

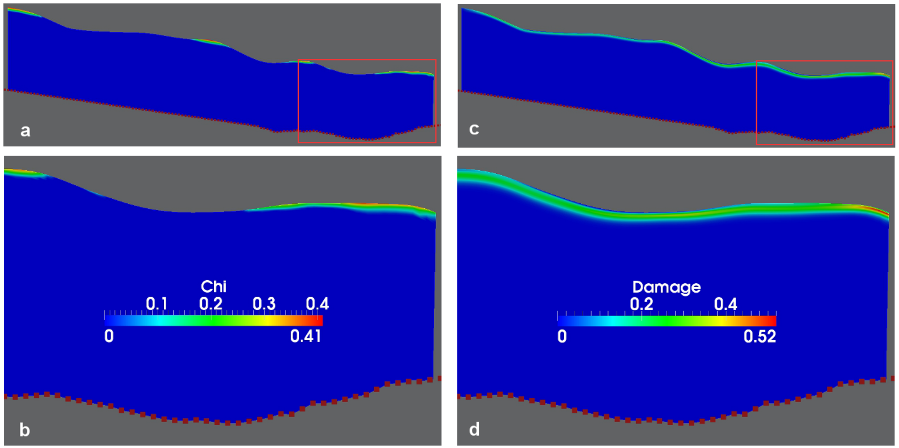

Fig. 8. State of Helheim glacier after 365 days of simulation for the set of parameter ($\overline{\sigma_{\text{th}}}$ = 0.072 MPa, B = 1.870 MPa^{-1}, and D_c = 0.529) corresponding to the red circle on Fig. 7. **(a)** Damaging areas of Helheim glacier and **(b)** zoom on the red rectangle; **(c)** damage field and zoom on the red rectangle **(d)**.

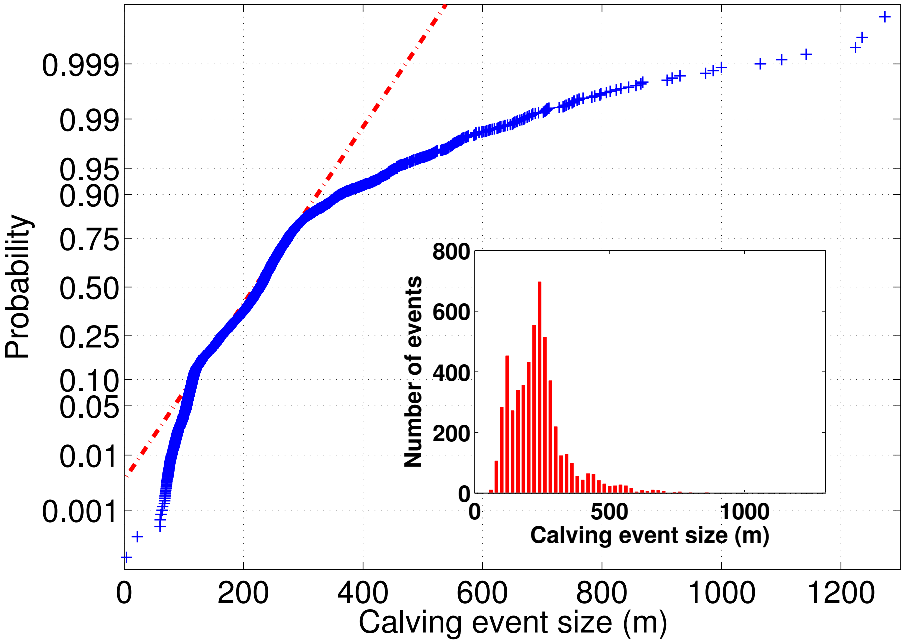

Fig. 9. Gaussian anamorphosis for the sizes of calving events corresponding to the 59 realistic simulations. Dashed-red curves represents the gaussian distribution associated with the calving event size distribution. Blue crosses correspond to individual events. The corresponding classical histogram is shown in the inset.

TCD
8, 1631–1671, 2014

Combining damage and fracture mechanics to model calving

J. Krug et al.